Minkowski-Voronoi diagrams as a method to generate random packings of spheropolygons for the simulation of soils

S. A. Galindo-Torres[*,†] and J. D. Muñoz[‡]

Simulation of Physical Systems Group, CeiBA-Complejidad, Department of Physics, Universidad Nacional de Colombia, Crr 30 No. 45-03, Ed. 404, Of. 348, Bogotá D.C., Colombia

F. Alonso-Marroquín[§]

School of Civil Engineering, The University of Sydney, Sydney, New South Wales 2006, Australia

Minkowski operators (dilation and erosion of sets in vector spaces) have been extensively used in computer graphics, image processing to analyze the structure of materials, and more recently in molecular dynamics. Here, we apply those mathematical concepts to extend the discrete element method to simulate granular materials with complex-shaped particles. The Voronoi-Minkowski diagrams are introduced to generate random packings of complex-shaped particles with tunable particle roundness. Contact forces and potentials are calculated in terms of distances instead of overlaps. By using the Verlet method to detect neighborhood, we achieve CPU times that grow linearly with the body's number of sides. Simulations of dissipative granular materials under shear demonstrate that the method maintains conservation of energy in accord with the first law of thermodynamics. A series of simulations for biaxial test, shear band formation, hysteretic behavior, and ratcheting show that the model can reproduce the main features of real granular-soil behavior.

PACS number(s): 47.11.Mn, 45.70.−n, 45.40.−f

I. INTRODUCTION

The study of soils, and granular materials in general, has attracted the attention of civil engineers who have to deal with settlement of buildings, earth pressure against retaining walls, stability of slopes and embankments, etc. The number of physicists interested in the subject has increased dramatically in recent years. A granular material is a typical example of a *complex system*: the collective macroscopic behavior of the system cannot be easily predicted from the microscopic nonlinear interactions of its constitutive elements. The constitutive equations (hypoplastic, viscoelastic, etc.) and phenomena (ratcheting, hysteresis, critical states, localization, etc.) governing soil mechanics at the macroscopic level have not been yet derived from the well-known grain shapes and microscopic forces among them. The solution of this problem has become an ultimate goal of soil mechanics, drawing together the efforts of geotechnical engineers and physicists.

Computer simulation has been one of the main tools for research on granular media. Discrete element methods, even in two dimensions, have given deep insights into the microscopic origin of such phenomena as ratcheting and strain localization, and there are many other aspects of the problem waiting to be explored through this paradigm. Two main discrete elements have been used for two-dimensional (2D) simulations: disks [1–3] and Voronoi polygons [4–8]. Disks are much simpler to describe, and their interaction laws are well enough known [1,9], but it is hard to capture with them all consequences of the irregular shapes of real grains. In contrast, Voronoi polygons [10,11] do capture such effects, but the interactions between grains are much more expensive to compute. Extensions to three dimensions are even harder because of the far greater difficulty in computing overlapping volumes between polyhedra.

An alternative for modeling complex shapes was proposed by Pournin and Liebling using Minkowski operations [12]. They introduced the concept of the spheropolyhedron, which is the Minkowski sum of a polyhedron and a sphere. Pournin and Liebling proposed a method to calculate contact interactions between spheropolyhedra based on a single contact for each pair of interacting particles. Later, Alonso-Marroquín introduced a method where the interaction is calculated using multiple contacts [13]. This multicontact method removed spurious oscillations of the particles and reduced the numerical production of kinetic energy, both of which were observed in the single contact model [14]. In two dimensions, the contact interactions among elements are always vertex-to-vertex or vertex-to-edge; in three dimensions, the contact interactions are vertex-to-face or edge-to-edge. These interactions can be modeled either lineally or with more accurate models [15,16], all of them with a well-defined elastic potential. 2D simulations on nondissipative systems showed accuracy in energy conservation with an error below 0.01%, while the energy balance for dissipative spheropolygons was not tested before. In the two-dimensional case, all dynamic properties of the discrete element—such as mass, center of mass, and moment of inertia—can be computed analytically, saving precious computer time. The contact interaction allows for optimization techniques like Verlet lists, which speed up the simulations between one and two orders of magnitude faster than those with clumps of spheres [14]. These discrete elements seem, therefore, very attractive for the numerical simulations of soils.

*Also at School of Civil Engineering, The University of Queensland, Brisbane QLD 4072, Australia.

†s.galinotorres@uq.edu.au

‡jdmunozc@unal.edu.co

§fernando.alonso@sydney.edu.au

This paper combines the Minkowski approach with the well-known and widely used Voronoi construction for random polygons to model granular materials with complex particle shapes. The idea can be further extended to three dimensions, and procedures for the three-dimensional case—also developed later—have been already published by one of the present authors [17]. Section II shows how to construct Voronoi spheropolygons using the concept of the Minkowski-Voronoi diagram. The section includes a review on Minkowski operators and the procedure to compute the dynamic properties of the spheropolygons. Section III introduces the interactions, elastic and dissipative, between spheropolygons and describes the numerical integration method used to evolve the system in time. Minkowski-Voronoi diagrams are used to simulate granular soils. In Sec. IV we perform a two-dimensional shear to test for energy balance and central processing unit (CPU) time. Once these benchmarks are successfully completed, the Minkowski-Voronoi spheropolygons are employed to simulate the biaxial tests under both monotonic and cyclic loadings. The simulations reproduce typical soil behaviors, such as strain localization on dense samples, emergence of a critical state for large strains, hysteresis loops on load-unload testing, and ratcheting as a persistent behavior upon cyclic loading.

II. VORONOI SPHEROPOLYGONS

Here, we introduce the geometrical construction of Voronoi spheropolygons to represent grains of complex shape. We review Minkowski operators and Voronoi diagrams, and we then combine these two geometrical methods to generate random packings of nonspherical particles. In addition, the dynamic properties (mass, center of mass, and moment of inertia) of these entities are computed for their further use as discrete elements.

A. Minkowski operators

Minkowski addition, along with the opening and erosion of sets, belongs to the area of mathematical morphology. These are tools for image processing, originally developed for the quantitative description of geological data from gray-level images [18]. Here, we present the definition of these operations in Euclidean spaces and apply them in building objects of complex shape and tunable particle roundness.

1. Dilation

Given two sets A and B in a Euclidean space, their Minkowski sum, or *dilation*, is defined by

$$A \oplus B = \{\vec{x} + \vec{y} | \vec{x} \in A, \vec{y} \in B\}. \tag{1}$$

This operation is geometrically equivalent to the profile obtained by sweeping one set around the other, without changing their relative orientation. This paper deals with spheropolygons, which are the Minkowski sum of a polygon with a disk (see Fig. 1). Other examples of Minkowski sum operations are the spherocylinder (sphere $\oplus$ line segment) [19], the Minkowski cow (nonconvex polygon $\oplus$ disk) [13], the spherosimplex (sphere $\oplus$ simplex) [12], and the
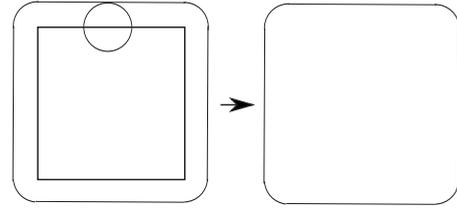

FIG. 1. Dilation of a square by a disk.

spheropolyhedron (sphere $\oplus$ polyhedron) [20].

2. Erosion

The erosion of set A by set B is defined over a Euclidean space by

$$A \ominus B = \{\vec{x} | B_{\vec{x}} \subseteq A\}, \tag{2}$$

where $B_{\vec{x}}$ is the translation of set B by the vector $\vec{x}$, that is,

$$B_{\vec{x}} = \{\vec{y} + \vec{x} | \vec{y} \in B\}. \tag{3}$$

Thus, the erosion of set A by set B can be understood as the locus of points reached by the center of set B when it moves inside set A. If set A is a polygon and set B is a disk of radius r, the erosion is a polygon inside set A whose borders lie at a distance r from the borders of set A (see Fig. 2).

3. Opening

The opening of set A by set B is obtained by the erosion of set A by set B, followed by dilation of the resulting image by set B,

$$A \circ B = (A \ominus B) \oplus B. \tag{4}$$

In our case, the opening of a polygon by a disk is the same polygon but with rounded corners (see Fig. 3). The degree of roundness increases as the radius of the disk does.

B. Voronoi-Minkowski construction

Voronoi spheropolygons are based on the Voronoi construction. This is a special decomposition of the Euclidean plane into disjoint convex polygons. They are generated by choosing at random a set of points, called Voronoi sites; each site $\vec{p}$ defines a Voronoi cell, consisting of all points on the plane closer to $\vec{p}$ than to any other Voronoi site. These cells are random polygons in size and shape that cover the plane without void spaces (Fig. 4). Constraints on the average area of polygons—and definite upper and lower limits on their areas—can be set by drawing a square tessellation on the
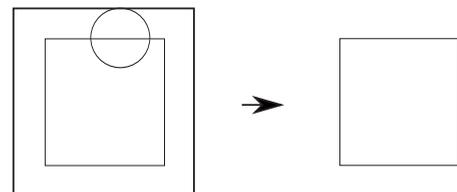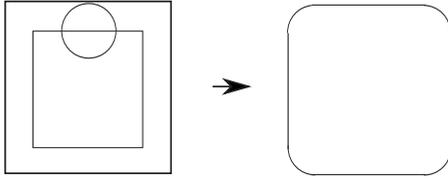

FIG. 2. Erosion of a square by a disk.

FIG. 3. Opening of a square by a disk.

plane and then choosing one Voronoi site at random within each square. The next step is to draw a spheropolygon W_i out of each Voronoi cell A_i. We first erode the cell by a disk B_d of radius d; then we apply a dilation on the eroded polygon by a disk B_R of radius R,

$$W_i = (A_i \ominus B_d) \oplus B_R. \tag{5}$$

The condition $R \le d$ guarantees that each spheropolygon is a subset of a Voronoi cell, and therefore that no spheropolygons overlap. If $R = d$, Eq. (5) reduces to the opening defined above. In this case, every border of each spheropolygon touches a border of another. Eroding a polygon can reduce the number of vertices, as we will show below. Let us start by drawing a *polygonal skeleton* inside the cell in such a way that each vertex $\vec{V}$ of this skeleton lies at exactly distance d from two different sides of the Voronoi cell. Assume that all vertices and edges of the Voronoi cell are numbered and oriented in the counterclockwise sense. For each vertex $\vec{x}$ of the Voronoi cell (see Fig. 5) there is a vertex candidate $\vec{x}_e$, given by

$$\vec{x}_e = \vec{x} + d \cot(\theta/2)\hat{e}_2 + d(\hat{k} \times \hat{e}_2), \tag{6}$$

where $\vec{x}$ is the intersection between the edges $\vec{E}_1$ and $\vec{E}_2$, $e_2 = \vec{E}_2 / \|\vec{E}_2\|$ is the unitary vector on the polygon edge, θ is the angle between the edges, and $\hat{k}$ is a unitary vector pointing out of the plane. Not all points satisfying Eq. (6) are vertices of the polygonal skeleton, only those farther than d from any other polygon side (Fig. 6). If all consecutive points $\vec{x}_e$ are
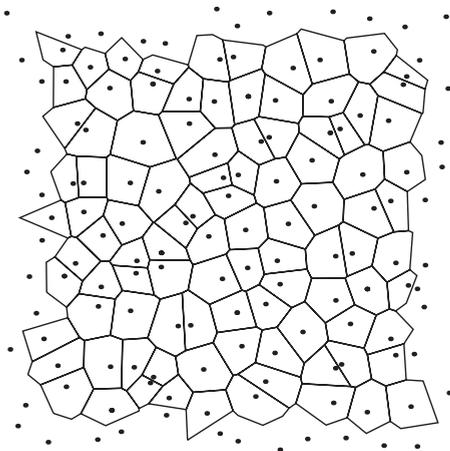

FIG. 4. A typical Voronoi construction in two dimensions. Exactly one Voronoi site (dot) is randomly generated within each square of a plane grid. Each Voronoi polygon is the set of points closer to a given site than to any other site.
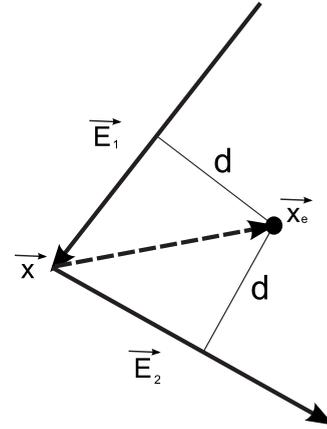

FIG. 5. For each vertex $\vec{x}$ of the Voronoi cell (see Fig. 4), one finds a vertex candidate $\vec{x}_e$ at a distance d of the cell edges intersecting at $\vec{x}$. The vectors $\vec{E}_1$ and $\vec{E}_2$ are two adjacent edges of the Voronoi polygon.

joined by lines, the intersections of such lines are the vertices of the desired polygonal skeleton V_i, which are now renumbered in the counterclockwise sense. The dilation of the polygonal skeleton V_i with the disk of radius R builds up the spheropolygon (Fig. 6). The Voronoi-Minkowski diagram is completed by performing the Minkowski operation described above [Eq. (5)] on all Voronoi cells. The result is shown in Fig. 7. The parameter R of Eq. (5) controls the initial volume fraction: the smaller is R, the larger is the void space between spheropolygons. The parameter d is a measure for spheropolygons' roundness: as d increases, the particles become more rounded. Therefore, the Voronoi-Minkowski construction allows us to generate random packings of particles with tunable void ratio and tunable roundness.

C. Dynamic properties

Let us compute the mass, center of mass, and moment of inertia of each spheropolygon. Consider the general case in Fig. 8, where the spheropolygon is divided into constitutive
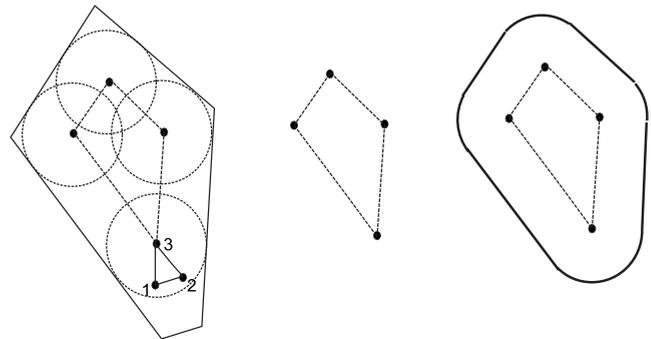

FIG. 6. The initial Voronoi cell A (left) is eroded by a disk element B_d of radius d. The eroded polygon $A \ominus B_d$ (center) is then dilated by the disk element B_R, producing the desired spheropolygon $(A \ominus B_d) \oplus B_R$ (right). Note the pathological case of points 1 and 2; since they are closer than d to another cell side, they are substituted by point 3.
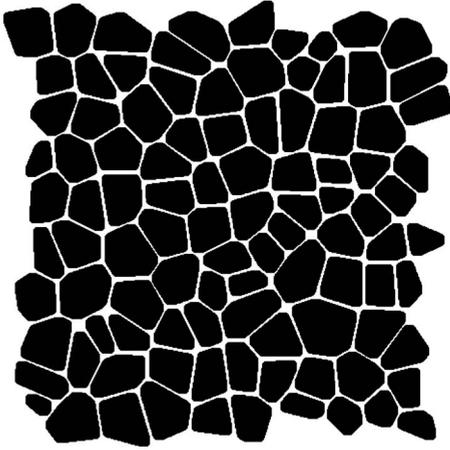
FIG. 7. An array of Minkowski-Voronoi spheropolygons constructed by the method described in the text. To allow void spaces between particles, the disk used for dilation is slightly smaller than the one used for erosion.

pieces: the polygonal skeleton at the center (in white), the rectangles of width R at the borders (in black), and the circular sectors of radius R at the vertices (in gray). The spheropolygons area, and therefore its mass, can easily be computed by summing the areas of its constituents. For each rectangle, this is just $A_r = L \times R$, where L is the length of the contiguous polygon side and R is the dilation radius. The area of each circular sector is $A_c = \frac{\beta}{2}R^2$, where $\beta = \pi - \theta$ is the supplement of the internal angle θ between the two corresponding polygon sides. The area of the central polygon is given by

$$A_p = \frac{1}{2}\sum_{i=0}^{n-1} (x_i y_{i+1} - x_{i+1} y_i), \tag{7}$$

with n as the number of sides and $\vec{V}_i = (x_i, y_i)$ as the coordinates of the ith vertex. The mass is computed by multiplying the total area by the surface mass density. Finding the center of mass of the spheropolygon starts by computing the center of mass of each sector. The rectangular sectors are the easiest for this task since for each the center of mass lies at its centroid. A circular sector has its center of mass on the bi-
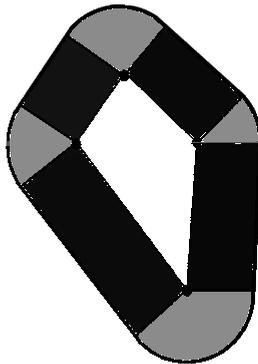

FIG. 8. Each spheropolygon is divided into regions to compute its mass properties.

sector line at a distance $d_{cm} = \frac{4R \sin(\beta/2)}{3\beta}$ from the circle center. The coordinates of the center of mass for the central polygon are

$$x_{cm} = \frac{1}{6A_p}\sum_{i=0}^{n-1} (x_i + x_{i+1})(x_i y_{i+1} - x_{i+1} y_i), \tag{8}$$

$$y_{cm} = \frac{1}{6A_p}\sum_{i=0}^{n-1} (y_i + y_{i+1})(x_i y_{i+1} - x_{i+1} y_i). \tag{9}$$

The coordinates of the total center of mass are weighted sums of the coordinates of the centers of mass of all its constituent sectors. We now compute the moment of inertia—a scalar quantity, because this is just a 2D problem. First we compute the moment of inertia for each region around its the center of mass. For the rectangles it is known that $I_r = \frac{1}{12}M_r(L^2 + R^2)$, with M_r as the rectangle mass. The moment of inertia for a circular sector is given by

$$I_c = \frac{M_c R^2 \{16[\cos(\beta) - 1] + 9\beta^2\}}{18\beta^2}. \tag{10}$$

The moment of inertia for the polygonal skeleton is

$$I_p = \frac{M_p \sum_{i=0}^{n-1} \|\vec{V}_i \times \vec{V}_{i+1}\|(V_i^2 + \vec{V}_i \cdot \vec{V}_{i+1} + V_{i+1}^2)}{6\sum_{i=0}^{n-1} \|\vec{V}_i \times \vec{V}_{i+1}\|}. \tag{11}$$

The overall moment of inertia is obtained by summing all of these moments using the Huygens theorem,

$$I_{\text{total}} = \sum_k (I_k + M_k r_k^2), \tag{12}$$

where the sum runs on all pieces, M_k and I_k are the mass and moment of inertia of the kth piece, and r_k is the distance between the center of mass of that piece and the overall center of mass. This completes the dynamic properties of the spheropolygon.

III. CONTACT LAWS

Most discrete element method (DEM) codes use similar numerical methods to integrate the equations of motion for the particle. The actual specific behavior is determined by the interaction forces among them. For granular materials, and in particular for soils, both elastic forces and dissipative terms are involved. Let us illustrate how these forces are implemented for spheropolygons.

A. Elastic forces

The spheropolygons differ from the Voronoi polygons [6] in that interaction among them is always between two circular vertices or between a circular vertex and an edge, obeying either a linear law or the well-known Hertz law. This rule is valid whenever the spheropolygons are stiff enough to avoid overlap between their polygonal skeletons. Let us take two

spheropolygons $W_i = P_i \oplus B_{r_i}$ and $W_j = P_j \oplus B_{r_j}$; that is, P_i and P_j are the respective polygonal skeletons of these spheropolygons. Each skeleton is defined by the sets of vertices $\{V_i\}$ and of edges $\{E_i\}$. To calculate the contact force between spheropolygons we consider all vertex-vertex and vertex-edge distances between P_i and P_j. For simplicity we use linear interactions. The force $\vec{F}(V_i, E_j)$ on the vertex V_i by the edge E_j is given by

$$\vec{F}(V_i, E_j) = K_n \delta(V_i, E_j) \vec{n}, \qquad (13)$$

where K_n is the elastic constant, $\delta(V_i, E_j)$ is the overlapping distance between the vertex and the edge [$\delta(V_i, E_j) = 0$ if there is no interpenetration], and $\vec{n}$ is a unitary vector perpendicular to the edge and is pointing out to the vertex. We assume that this force is exerted in the middle point $\vec{r}(V_i, E_j)$ on the line segment from the vertex to (and orthogonal to) the edge. Thus, the torque resulting from this force on the spheropolygon i is

$$\vec{\tau}(V_i, E_j) = [\vec{r}(V_i, E_j) - \vec{r}_i^{\text{cm}}] \times \vec{F}(V_i, E_j), \qquad (14)$$

where $\vec{r}_i^{\text{cm}}$ is the center of mass of the spheropolygon i. Similarly, the force $\vec{F}(V_i, E_j)$ on the vertex V_i by the vertex V_j is given by

$$\vec{F}(V_i, V_j) = 2 K_n \delta(V_i, V_j) \vec{n}, \qquad (15)$$

where $\delta(V_i, V_j)$ is the interpenetration distance between them [$\delta(V_i, V_j) = 0$ if there is no interpenetration] and $\vec{n}$ is a unitary vector pointing out from V_i to V_j. We also assume that this force is exerted in the middle point $\vec{r}(V_i, V_j)$ on the line segment between the two vertices. Thus, the torque resulting from this force on the spheropolygon i is

$$\vec{\tau}(V_i, V_j) = [\vec{r}(V_i, V_j) - \vec{r}_i^{\text{cm}}] \times \vec{F}(V_i, V_j). \qquad (16)$$

The force $\vec{F}_{ij}$ acting on the spheropolygon i by the spheropolygon j is just the sum of all forces between vertices at i and edges at j plus all forces between vertices at j and edges at i and all forces between vertices at j and vertices at i,

$$\vec{F}_{ij} = -\vec{F}_{ji} = \sum_{V_i E_j} \vec{F}(V_i, E_j) + \sum_{V_j E_i} \vec{F}(V_j, E_i) + \sum_{V_i V_j} \vec{F}(V_i, V_j). \qquad (17)$$

In a similar way, the torque resulting from these forces is given by

$$\vec{\tau}_{ij} = \sum_{V_i E_j} [\vec{r}(V_i, E_j) - \vec{r}_i^{\text{cm}}] \times \vec{F}(V_i, E_j) + \sum_{V_j E_i} [\vec{r}(V_j, E_i) - \vec{r}_i^{\text{cm}}]$$
$$\times \vec{F}(V_j, E_i) + \sum_{V_j V_j} [\vec{r}(V_j, V_j) - \vec{r}_i^{\text{cm}}] \times \vec{F}(V_i, V_j). \qquad (18)$$

So computing forces and torques between spheropolygons is extremely simple. It asks neither for overlapping areas between polygons nor for Minkowski operators. As pointed out before, another advantage is the simple way the energy can be computed. Since the force is basically a spring force, the potential energy U associated with each contact can be taken as

$$U(E_i, V_j) = \tfrac{1}{2} K_n \delta^2(E_i, V_j), \qquad (19)$$

for the contact between edge E_i and vertex V_j. This expression will be used later in testing for energy balance.

B. Frictional and viscous forces

For the examples presented in this paper we introduced frictional forces by using the method proposed by Cundall and Strack [1]. The frictional force $\vec{F}_f$ is taken as proportional to the tangential displacement,

$$\vec{F}_f(V, E) = K_t \delta_t \vec{t}, \qquad (20)$$

where $\vec{t}$ is the tangential vector defined by $\vec{n}$ to $\vec{n}$. The elastic displacement δ_t is the time integral of the tangential component of the relative velocity at the contact point [21]. The coefficient K_t is the tangential stiffness (analogous to K_n for the normal direction). This contact force satisfies the sliding condition $F_f = \min\{\mu K_n \delta, K_t |\delta_t|\}$, where μ is the static friction coefficient. Hence, when δ_t reaches the threshold value, F_f takes the Coulomb limit. Since the tangential force is elastic before this limit, it also has a potential energy given by

$$U(E_i, V_j) = \tfrac{1}{2} K_t \delta_t^2. \qquad (21)$$

Viscosity forces proportional to the relative velocity of the contacts are also included to allow the system to relax. For our case, we take

$$\vec{F}_v(V, E) = -G_n m_e v_n \vec{n} - G_t m_e v_t \vec{t}, \qquad (22)$$

where the force depends on two dissipative constants for the normal (G_n) and tangential (G_t) directions, m_e is the reduced mass for the two particles, and v_n, v_t are the components of the relative velocity $\vec{v}_r = v_n \vec{n} + v_t \vec{t}$ at the contact point. These equations of motion are numerically solved by using a fourth-order predictor-corrector algorithm [22].

IV. SIMULATION BENCHMARKS

To investigate the computer performance of the Voronoi spheropolygons we simulate a two-dimensional shear band with periodic boundary conditions (Fig. 9). The polygons are confined by two horizontal plates: the lower plate is fixed and the upper one exerts a constant vertical pressure and moves at a constant horizontal speed. The left and right boundaries are periodic. The simulations are performed on a sample of 60 particles. The particles are first constructed from a Minkowski-Voronoi diagram of 6×10 grains; next, they are placed on the nodes of a larger square array and rotated at random, and finally they are consolidated by both the action of gravity and the action of the upper plate. The parameters of the simulations are as follows: normal stiffness $K_n = 1 \times 10^4$ dyn/cm, tangential stiffness $K_t = 0.33 K_n$, normal and tangential coefficients of viscosity $G_n = 16$ s^{-1} and $G_t = 4$ s^{-1}, friction coefficient $\mu = 0.4$, density $\rho = 3$ g/cm^2, gravitational acceleration $g = 10$ m/s^2, and time step $\Delta t = 0.001$ s. The mean of the diameter of the particles is $\ell = 0.76$ cm and the default value of the erosion radius is $R = 0.1$ cm.
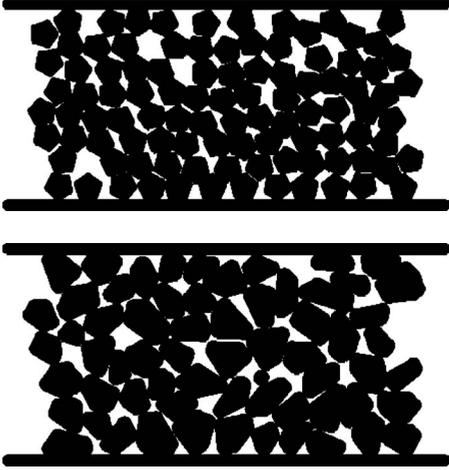
FIG. 9. Snapshot of shear-cell simulation with regular sphero-pentagons (above) and Minkowski-Voronoi spheropolygons (below).
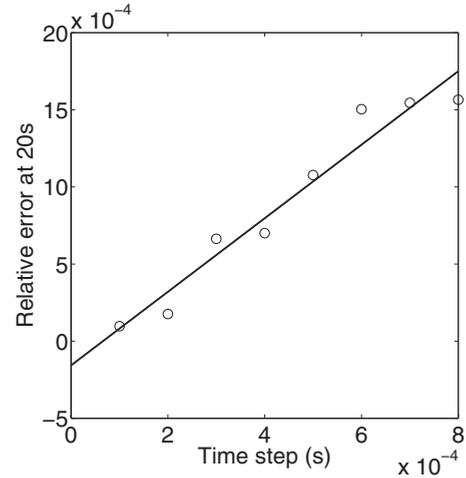

FIG. 10. Relative error in the energy balance versus time step (in units of seconds) in simulation of shear cells with Minkowski-Voronoi spheropolygons.

A. Energy balance test

In numerical simulation of dissipative systems, the energy balance is tested by calculating the input of energy to the system and verifying that it corresponds to the change of the sum of the potential, kinetic, and dissipated energies [23]. Strictly speaking, no numerical method satisfies this energy balance, because the systematic errors of the numerical integration accumulate with time. If the numerical error decreases when the time step is reduced, the integration method is said to be *consistent*. This consistency is rarely discussed in DEM modeling. Pöschel [11] discussed an example of interacting polygons where consistency cannot be verified: if the force is calculated as a function of the overlap between polygons, there is no expression for potential energy, so there can be no energy balance equations. Pöschel proposed calculating the potential energy in terms of overlapping lengths, which leads to an elastic contact force that is quite complex and difficult to extend to three dimensions. These complications are avoided with spheropolygons, because the elastic forces are derived from well-defined potentials, as discussed in the previous section.

As a first test, let us check if the energy balance holds, as established by the first law of thermodynamics (work done on the system=energy dissipated+increase in internal energy). Figure 10 shows the energy difference ratio after a constant time of 20 s for time steps of several lengths. The ratio is computed as $\frac{E+Q-L}{E}$, with E as the sum of the kinetic and gravitational potential energies of the particles plus the elastic energy at the contacts, Q as the energy dissipated by frictional and viscous forces, and L as the work exerted by the walls.

The error in the energy balance grows linearly with the length of the time step, which shows that the numerical method is consistent. It is remarkable that the error is on the order of $O(\Delta t)$, while we are using a fourth-order method to solve the equations of motion. We also notice that the error can reach 0.2% for frictional materials, while it is well below 0.01% for nonfrictional materials [14]. The main reason for

the numerical error is that friction forces are calculated incrementally, and therefore introduce errors on the order of $O(\Delta t^2)$ in each time step. Future work therefore needs to be done to achieve more accurate simulations in frictional materials. In spite of this error, our model is still numerically consistent, and it is suitable for problems that require a precise energy balance, such as the calculation of heat produced in shear bands and the increase in the temperature due to frictional forces. This important advantage is a direct consequence of defining a proper elastic potential energy at the contacts that was not available in previous models that used polygons [10,11].

B. CPU optimization

Since most of the CPU time of the simulation is spent in the calculation of the contact forces, the major reduction in the computational effort can be achieved by computing the forces only on those vertex-edge or vertex-vertex pairs that are relatively close to each other. With this aim we introduce a *neighbor list* of all pair particles closer than 2α. The constant α is equivalent to the *Verlet distance* proposed by Verlet to speed up simulations with spherical particles [24]. A *link cell* algorithm [11] is used for a rapid construction of the Verlet list. For each element of the Verlet list, we create a *contact list*, consisting of those vertices and edges in pair particles of the Verlet list that are closer than $R_i+R_j+2\alpha$, with R_i and R_j as the dilation radii of the corresponding particles. In each time step, only the vertex-vertex and vertex-edge pairs in the contact list are involved in computing the contact forces. These lists make only small demands on memory storage. All lists are updated when the displacement of any point at any particle surpasses the value α.

First we investigated how the simulation time depends on the number of vertices of the spheropolygons. We measured the CPU time required to simulate 20 s of the shear band evolution by using regular spheropolygons with different numbers of sides. We started with triangles and ended with heptagons. The results are shown in Fig. 11. With α=0.9 the
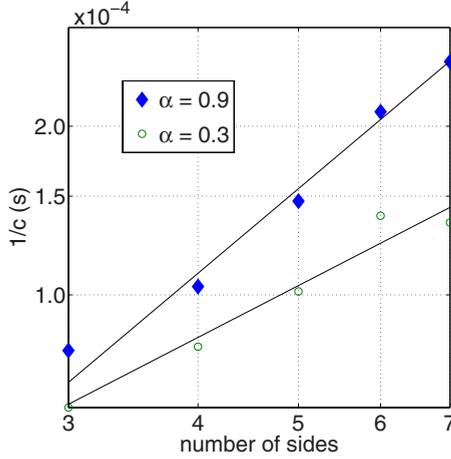
FIG. 11. (Color online) Inverse of the Cundall number (in units of seconds) versus number of vertices of the regular spheropolygons employed for the simulation of the shear band (log-log scale). When the Verlet lists are almost switched off ($\alpha=0.9$), one observes a power-law dependence with exponent 1.56(23). Switching on the optimization scheme by taking $\alpha=0.3$ reduces this exponent to a linear relationship [exponent 0.98(31)].

Verlet list is not frequently updated and the optimization is for all purposes turned off. Computing the force is then the predominant load, and the normalized CPU time grows with the number of sides as a power law with an exponent 1.56(23). Reducing α decreases the CPU demand to compute the forces, and the exponent of this power law reduces to 0.98(31), i.e., a linear relationship.

As we stated above, the total CPU time is mainly split into computing the forces and updating the Verlet lists. We propose a power-law dependence for both terms,

$$T_{CPU} = \frac{A}{\alpha^{\beta}} + B\alpha^{\gamma}, \tag{23}$$

where A, B, β, and γ are fitting parameters. Figure 12 shows this fitting for $\beta=0.704$, $\gamma=0.3573$, $A=4.34e-7$, and $B=9.91e-5$. One concludes that choosing an optimum value for α ensures a considerable saving in CPU time.

V. BIAXIAL TEST

A. Monotonic load

As an application of the Minkowski-Voronoi diagrams to soil mechanics, we simulated a biaxial test. In our setup, four walls enclose a sample of 30×40 spheropolygons. First an isotropic stress of $\sigma_a=0.256K_n$ is applied on all walls. Next, a constant strain rate condition is imposed on the upper and lower walls by fixing a vertical speed of 0.001 m/s while the axial stress σ_l is measured. The test is performed for two initial states: a dense sample obtained with the original closed packing of Voronoi polygons and a loose one constructed by expanding the closed packing and rotating each particle at random before the isotropic compression starts. Figure 13(a) shows the deviatoric stress $q=(\sigma_a-\sigma_l)$ as a function of the axial strain for both initial loose and dense
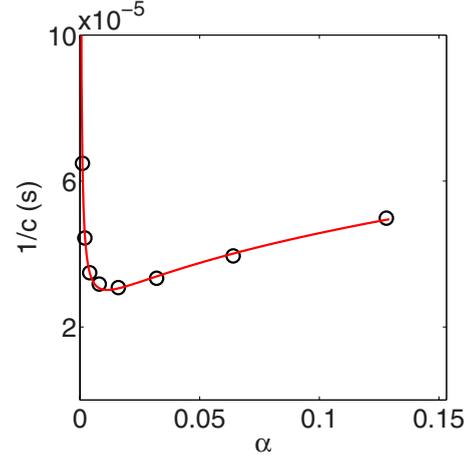

FIG. 12. (Color online) Normalized CPU time versus Verlet distance α (in centimeters) for the simulation of a shear cells with Minkowski-Voronoi spheropolygons. The model of Eq. (23) fits this dependence quite well, with parameters $\beta=0.704$, $\gamma=0.3573$, $A=4.34\times10^{-7}$, and $B=9.91\times10^{-5}$.

states. For dense samples q increases until it reaches a peak (the failure point) and then it decays to a constant value. For loose samples q increases monotonically, but both loose and dense tests converge to the same final value, which characterizes the so-called *critical state* [23,25]. At this state, the volumetric strain is also constant, as shown in Fig. 13(b). The stress ratio and the void ratio at the critical state are fundamental quantities that characterize the material since they are independent on the way the soil is prepared.

Now we compare our simulations with spheropolygons to the study by Alonso-Marroquin and Herrmann on Voronoi polygons [6]. Let us plot the deviatoric stress q_f at the failure point as a function of the confining pressure p_f. The results can be seen in Fig. 14. We observe a power-law dependence, with an exponent 0.85(2) that deviates from the linear relationship predicted by the Mohr-Coulomb failure criterion. The exponent is larger than the value of 0.93 observed with Voronoi polygons. This result supports the idea that the Coulomb criterion is not an accurate description for the failure of the material, because the friction angle changes with the confining pressure and is not a material parameter.

We tested whether the spheropolygons behave like a common dry soil upon failure. We proceeded to checking the Mohr-Coulomb criterion for the orientation of the shear band. The shear band was revealed by plotting at the failure point the cumulated displacement for each polygon from its initial position [Fig. 15(a)]. We measured the orientation angle θ of the shear bands and compared it with the ones predicted by the Mohr-Coulomb criterion [6]

$$\theta_{MC} = 45° + \arcsin(q_f/p_f)/2, \tag{24}$$

and the Roscoe criterion [26]

$$\theta_R = 45° + \arctan(d\epsilon_v/d\epsilon_d)/2 \tag{25}$$

[Fig. 15(b)]. As in previous studies with Voronoi polygons [10], the error bars we obtain are too wide (a consequence of
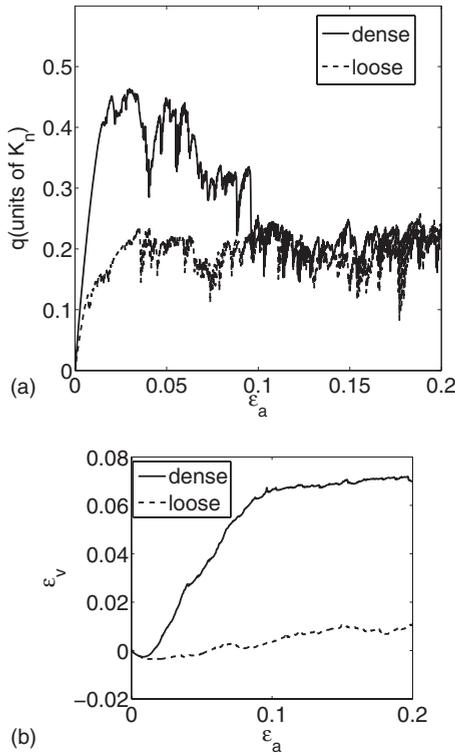
FIG. 13. (a) Deviatoric stress q and (b) volumetric strain ϵ_v as functions of the axial strain ϵ_a for both a dense (continuous line) and a loose (dashed line) packing of 1200 spheropolygons under a biaxial test (horizontal confining pressure $\sigma_a = 0.256 K_n$ and vertical constant strain rate $\dot{\epsilon}_l = 0.005/\text{s}$).

the small number of elements), but in agreement with both criteria.

We will now investigate the failure properties of the Voronoi spheropolygons as a function of their particle roundness. Following normal practice, we use Mohr-Coulomb circles to represent the failure limit of sheared granular materials at different values of pressure. These circles are plotted in the τ-σ plane, where τ is the shear stress and σ is the
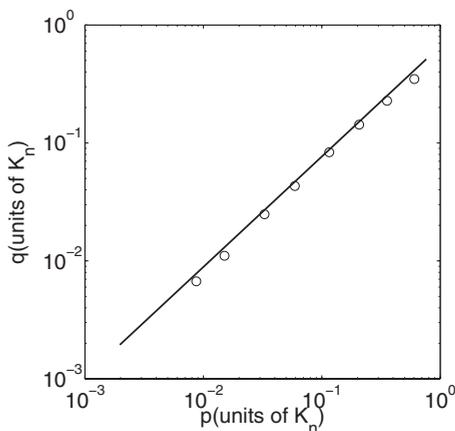

FIG. 14. Deviatoric stress at failure as a function of the confining pressure. A nonlinear power dependence, with exponent 0.85(2), is obtained, in contrast with the linear relationship established by the Mohr-Coulomb failure criterion.
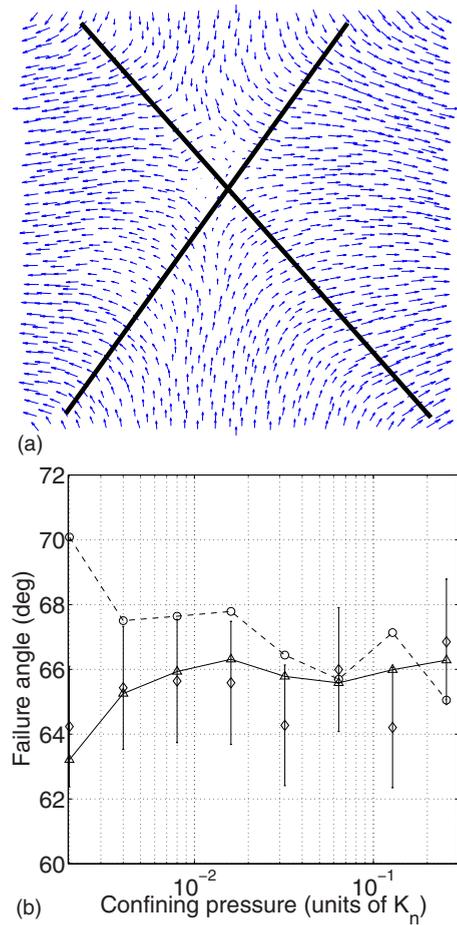

FIG. 15. (Color online) (a) (Color online) The shear bands are identified by plotting the cumulated displacement vector for each spheropolygon. (b) The measured shear band orientations (diamonds) for several confining pressures, compared with those predicted by the Mohr-Coulomb (circles) and the Roscoe (triangles) criteria.

normal stress. The center of the Mohr-Coulomb circle is the confining pressure p, and its radius is the deviatoric stress q. The envelope of the circles at failure defines the so-called Mohr-Coulomb failure line, which is approximated by a straight line $\tau = \sigma \tan \phi$, where ϕ is the angle of friction.

Figure 16 shows the failure line for different values of particle roundness. The roundness is given by the erosion radius, which is kept equal to the dilation radius. (The erosion radius and dilation radius are defined in Sec. II.) For erosion radii of 0.5, 1, and 1.5 mm the angles of friction are 60°, 58°, and 51°. In other words, the more angular the particles are, the greater is the strength of the granular material. The results are in agreement with three-dimensional simulations on spheropolyhedra [27], which show that the angle of friction decreases as the particle is more rounded. In general there are two geometrical issues affecting friction: the interlocking due to convexity [27] and the capacity of the particles to release stress by rolling [28]. The second of these is directly linked to the angularity of the particle, as shown in our simulations with spheropolygons.
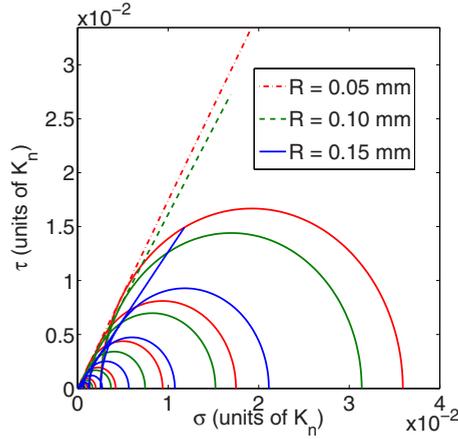
FIG. 16. (Color online) Mohr-Coulomb failure line for Voronoi spheropolygon packings with three different erosion parameters: r =0.5, 1, and 1.5 mm. Each failure line is the envelope of the Mohr circles at failure (curves in the figure). As erosion is larger the strength of the packing decreases.

B. Harmonic load

Having tested the response under monotonic loads, let us study the response of the spheropolygons under cyclic loads. The modification in our experimental setup is very simple. The cyclic loading is achieved by adding a harmonic pressure on the horizontal walls, and the axial stress becomes

$$\sigma_a(t) = p_0 + \Delta\sigma[1 + \cos(2\pi t/T)]/2, \qquad (26)$$

with p_0 as the confining pressure, T as the period, and $\Delta\sigma$ as the amplitude of the harmonic oscillation. Only at very low stress amplitudes the soil response is elastic, drawing a single path in the stress-strain diagram. In general, the response draws a *hysteresis loop*, as shown in Fig. 17(a). The area of the hysteresis loop is related to the amount of plastic dissipation. By looking at the first cycle, Fig. 17(b) shows how the area of the hysteresis loop grows with the amplitude of the oscillation. After a certain amplitude the area grows rapidly, and the sample is said to surpass the *shakedown* limit [29], where ratcheting appears (see below). The plot of the hysteresis area versus amplitude in [Fig. 17(b)] helps us to estimate this value around $0.2p_0$ for our sample.

The increase in the hysteresis loop area with the loading amplitude is predicted by the elastoplastic theory. For small amplitudes the deformation is basically elastic, and the area of the hysteresis loop is relatively small because of the small loss in energy. However, once the loading amplitude increases, the energy lost by internal friction takes a larger portion of the total energy and drives an irreversible deformation. A model proposed by Karg and Haegeman [30] introduces a relationship between the stress σ_m and the strain ϵ_m at the tip of the hysteresis loop and the hysteresis area A_{loop}. It is expressed in terms of the damping coefficient D,

$$D = \frac{A_{\text{loop}}}{A_\Delta}, \qquad (27)$$

with A_Δ as the area of the right-angled triangle drawn from the origin to the tip. For a completely elastic material D
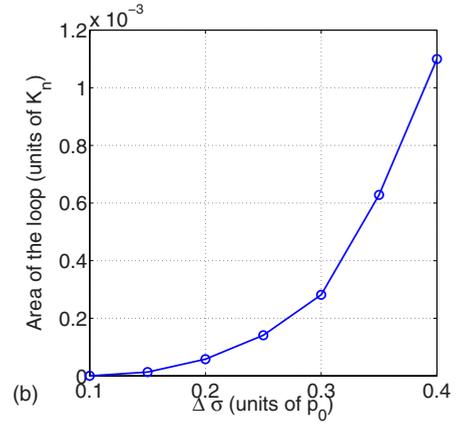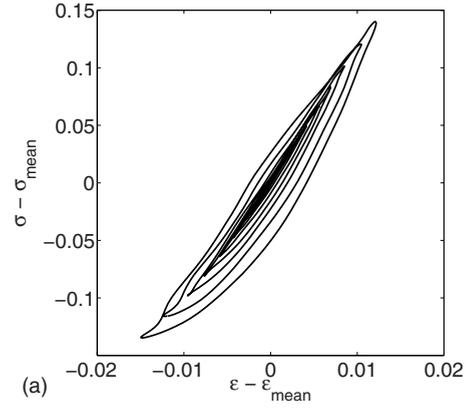

FIG. 17. (Color online) (a) The hysteresis loops for different oscillation amplitudes in the stress-strain space. The stress difference is given in units of p_0. (b) Hysteresis area versus amplitude.

should be zero, but plastic deformation brings a positive value for D. The relationship is written as

$$D = D_{max}\left(1 - \frac{\sigma_m}{E_{max}\epsilon_m}\right), \qquad (28)$$

where D_{max} is the maximum damping coefficient and E_{max} is the maximum tensile modulus. The physical meaning of D_{max} is the following: at large values of ϵ_m, σ_m does not grow anymore since the system is in the plastic deformation regime; therefore, the ratio $\sigma_m/E_{max}\epsilon_m$ goes to zero and D takes the maximum damping value for the soil. In contrast, E_{max} indicates the maximum measurable tensile modulus before the soil enters into the plastic regime.

Figure 18 fits this model to the simulation data. The correlation factor is 97%. The fitting parameters are D_{max} =5.22(5) and E_{max}=11.3(4). The good agreement shows the consistence of our model with the cyclic loading response of granular soils.

Let us check next for an important consequence of elastoplasticity at cyclic loading, i.e., the granular ratcheting that has been reported from triaxial tests [30]. In this phenomenon the sample accumulates strain after each loading cycle, getting an increasing permanent deformation with time. Figure 19 shows how the Minkowski-Voronoi packing of 30 ×40 elements accumulates strain by each cycle.
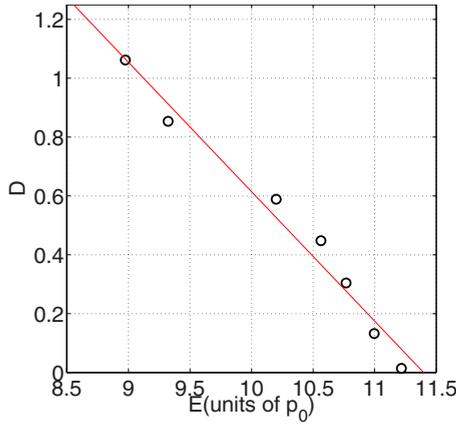
FIG. 18. (Color online) Damping coefficient D versus tensile modulus $E = \sigma_m / \epsilon_m$.

Now we explore the dependence of ratcheting on the loading amplitude. For this purpose we calculate the mean accumulated strain per cycle once the asymptotic state shown in Fig. 19(a) is reached. The results are plotted in Fig. 19(b). Above an amplitude of $0.2K_n$ the rate of accumulated strain increases rapidly (Fig. 20). Many researchers call this value the shakedown limit [31], where the soil starts accumulating plastic deformation with each cycle.

There is a recent controversy regarding the origin of granular ratcheting in DEM simulations. McNamara *et al.* [32] showed that ratcheting in simulations of disks or spheres may appear as a numerical effect of the nonconservation of elastic energy of Cundall's model of friction. Figure 21 shows the origin of this numerical ratcheting. Consider a
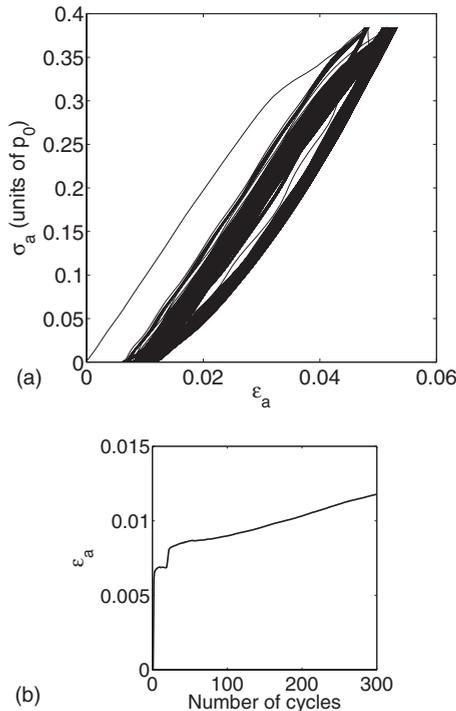

FIG. 19. (a) The relation between the axial stress and axial strain and (b) the accumulated strain at each cycle showing granular ratcheting.
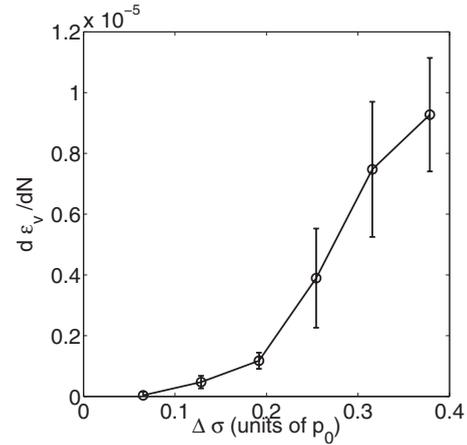

FIG. 20. Accumulated strain per cycle versus the oscillation amplitude.

disk colliding with another one, as in Fig. 21 (left), and assume that the contact point draws the path CABD, with the segment DC larger than the segment AB. The static friction in the Cundall model is a tangential spring force that is proportional to these lengths, so the work performed on the segment DC becomes larger than on the segment AB. The total work of this elastic force on the closed path CABD becomes negative, and an amount of mechanical energy is lost at every cycle. McNamara *et al.* [32] proposed a force-displacement relation to correct this effect, with the consequence that the ratcheting vanishes. In the case of spheropolygons we have two kinds of interactions. Vertex-vertex interactions show the same problem McNamara *et al.* pointed out for disks, but vertex-edge interactions do not. Figure 21 (right) shows that in the last case the closed path draws a rectangle, so the Cundall frictional force is conservative on this path and the problem does not arise. In our simulation the number of vertex-vertex interactions is less than 20% of all interactions.

To confirm this relation between particle roundness and ratcheting, we perform three series of cyclic loading simulations using different erosion parameters: $R = 0.5$, 1, and 1.5 mm. The average of the results on eight samples is shown in Fig. 22. As the particles are more rounded, the ratcheting becomes larger. This is consistent with the increase in vertex-vertex contacts when the erosion radius is increased. These preliminary results suggest that the McNamara ratcheting may play an important role for circular particles. Different mechanisms of ratcheting may appear when the particles are highly angular. In light of previous ratcheting simulations of polygons that also showed ratcheting [31], we conclude that the McNamara ratcheting is not the unique microscopic mechanism of permanent accumulation of plastic deformation on cyclic loading. In the general case, ratcheting arises when the loops of the contact forces are not exactly closed during the cyclic loading. This point concerning the microscopic origin of open contact force loops in angular particles demands further study.
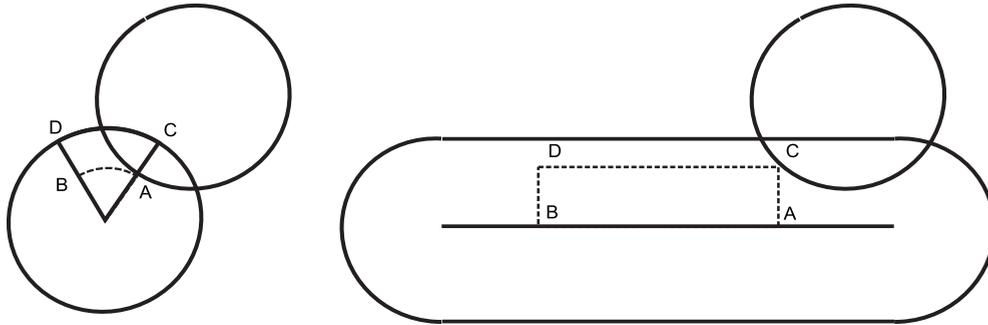
FIG. 21. The origin of numerical ratcheting in a spheropolygon. Left: a closed ABCD loop in the trajectory of the contact leads to a spurious change in potential energy, as shown by McNamara *et al.* [32]. The reason is that the energy stored in AB is not the same as the energy released in CD. This spurious energy is absent in vertex-edge contacts (right), because AB and CD have the same length. Therefore, the spheropolygons only partially solve the problem of numerical ratcheting.

VI. CONCLUDING REMARKS

We have shown how to combine the Minkowski operators with the Voronoi diagrams in two dimensions to construct Minkowski-Voronoi spheropolygons that are suitable to model granular soils. The spheropolygons unite consideration of the random shape of 2D Voronoi polygons with the well-defined forces and elastic potentials of interactions among disks. This allows for more realistic simulations of soils while preserving the ability to test for energy balance. Numerical tests show that the use of Minkowski-Voronoi spheropolygons reproduces the main features of the biaxial test for dense and loose samples, including the emergence of an asymptotic critical state. They also account for the formation of shear bands with the proper orientation, the onset of ratcheting, and the presence of hysteresis loops in agreement with empirical models.

The mass, center of mass, and moment of inertia of spheropolygons are computed analytically, in comparison with the three-dimensional case (already published in [17]), where such quantities are computed by Monte Carlo methods. The simulation is further accelerated by building a Verlet list, whose individual elements are the potential vertex-edge contacts between particles. This construction reduces

the CPU time to compute the contact forces to $O(M)$, where M is the number of vertices of the spheropolygons. We calculated the components of energy in simulations of dissipative spheropolygons. The energy balance is achieved with around 0.2% accuracy. Comparing this result to the error of 0.01% for energy in nondissipative spheropolygons, we conclude that the time integration of friction forces is a major source of error. Nevertheless, we demonstrated the consistency of the numerical method, as the error decreases by reducing time steps as $O(\Delta t)$. This result makes the spheropolygons suitable for the study of soil phenomena where this balance plays a major role, as in hysteresis, ratcheting, heating of the intergranular water inside a shear band, or an increase in the rock temperature due to frictional forces. These problems are subjects of interest for future work.

Cyclic loading simulations with Voronoi spheropolygons show that the model responds as much as actual granular soils do. Ways in which results agree with experiments include the existence of the shakedown limit, the nested structure of hysteresis loops when different loading amplitudes are taken, and the emergence of granular ratcheting for moderate amplitudes of cyclic loading. The amount of ratcheting observed with angular particles is much lower than with rounded particles. The accumulation of ratcheting on vertex-vertex contacts is consistent with the limitations of the Cundall model of friction as discussed by McNamara *et al.* This friction model, widely used for modeling granular material, is prone not only to numerical integration error but also to spurious ratcheting. Future research on energetics and cyclic loading in dissipative granular materials would do well to revisit the current model of friction in discrete element simulations.
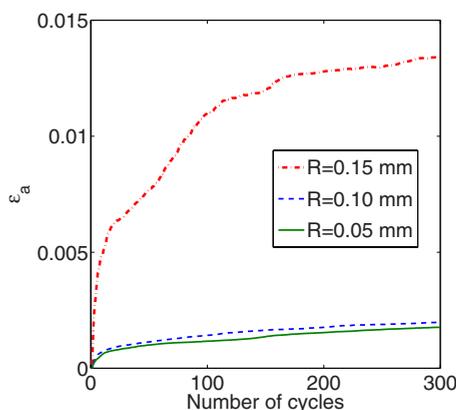

FIG. 22. (Color online) Permanent accumulation of plastic deformation versus the number of cycles for three different particle roundness. The roundness is defined by the erosion parameters, which are taken as $r=0.5$, 1, and 1.5 mm.

[1] P. A. Cundall and O. D. L. Strack, Geotechnique **29**, 47 (1979).

[2] H. Kruggel-Emden, E. Simsek, S. Rickelt, S. Wirtz, and V. Scherer, Powder Technol. **171**, 157 (2007).

[3] S. D. C. Walsh, A. Tordesillas, and J. F. Peters, Granular Matter **9**, 337 (2007).

[4] H. J. Tillemans and H. J. Herrmann, Physica A **217**, 261 (1995).

[5] F. Kun and H. J. Herrmann, Comput. Methods Appl. Mech. Eng. **138**, 3 (1996).

[6] F. Alonso-Marroquin and H. J. Herrmann, Phys. Rev. E **66**, 021301 (2002).

[7] J. A. Åström, B. L. Holian, and J. Timonen, Phys. Rev. Lett. **84**, 3061 (2000).

[8] S. A. Galindo Torres and J. D. Muñoz Castaño, Phys. Rev. E **75**, 066109 (2007).

[9] S. Luding and H.-G. Matuttis, *Friction, Arching and Contact Dynamics* (World Scientific, Singapore, 1997), pp. 373–376.

[10] F. Alonso-Marroquin, S. Luding, H. J. Herrmann, and I. Vardoulakis, Phys. Rev. E **71**, 051304 (2005).

[11] T. Pöschel and T. Schwager, *Computational Granular Dynamics* (Springer, Berlin, 2004).

[12] L. Pournin and T. M. Liebling, *Powders & Grains 2005* (Balkema, Leiden, 2005), pp. 1375–1478.

[13] F. Alonso-Marroquin, EPL **83**, 14001 (2008).

[14] F. Alonso-Marroquín and Y. Wang, Granular Matter **11**, 317 (2009).

[15] T. Schwager and T. Pöschel, Granular Matter **9**, 465 (2007).

[16] M. J. Puttock and E. G. Thwaite, National Standards Laboratory Technical Report No. 25, 1969 (unpublished).

[17] S. A. Galindo-Torres and D. M. Pedroso, Phys. Rev. E **81**, 061303 (2010).

[18] J. Serra, *Image Analysis and Mathematical Morphology* (Academic Press, Inc., Orlando, FL, 1983).

[19] L. Pournin, M. Weber, M. Tsukahara, J.-A. Ferrez, M. Ramaioli, and Th. M. Liebling, Granular Matter **7**, 119 (2005).

[20] L. Pournin, Ph.D. thesis, École Polytechnique Fédérale de Lausanne, 2005.

[21] R. García-Rojo, F. Alonso-Marroquín, and H. J. Herrmann, Phys. Rev. E **72**, 041302 (2005).

[22] C. W. Gear, *Numerical Initial Value Problems in Ordinary Differential Equations* (Prentice Hall PTR, Upper Saddle River, NJ, 1971).

[23] F. Alonso-Marroqun, I. Vardoulakis, H. J. Herrmann, D. Weatherley, and P. Mora, Phys. Rev. E **74**, 031306 (2006).

[24] L. Verlet, Phys. Rev. **159**, 98 (1967).

[25] D. M. Wood, *Soil Behaviour and Critical State Soil Mechanics* (Cambridge University Press, Cambridge, England, 1990).

[26] P. A. Vermeer, Geotechnique **40**, 223 (1990).

[27] S. A. Galindo-Torres, F. Alonso-Marroquín, Y. C. Wang, D. Pedroso, and J. D. Muñoz Castaño, Phys. Rev. E **79**, 060301 (2009).

[28] Akke S. J. Suiker and Norman A. Fleck, ASME Trans. J. Appl. Mech. **71**, 350 (2004).

[29] S. Werkmeister, A. R. Dawson, and F. Wellner, J. Trans. Engrg **130**, 665 (2004).

[30] C. Karg and W. Haegeman, Soil Dyn. Earthquake Eng. **29**, 155 (2009).

[31] F. Alonso-Marroquin and H. J. Herrmann, Phys. Rev. Lett. **92**, 054301 (2004).

[32] S. McNamara, R. García-Rojo, and H. J. Herrmann, Phys. Rev. E **77**, 031304 (2008).